(This is a sample cover image for this issue. The actual cover is not yet available at this time.)

Journal of Non-Newtonian Fluid Mechanics 195 (2013) 32–45

Contents lists available at SciVerse ScienceDirect

Journal of Non-Newtonian Fluid Mechanics

journal homepage: http://www.elsevier.com/locate/jnnfm

Numerical simulation of thermal plumes in a Herschel–Bulkley fluid

Anna Massmeyer [a,*], Erika Di Giuseppe [a,b], Anne Davaille [a], Tobias Rolf [c], Paul J. Tackley [c]

[a] Laboratoire FAST (CNRS/UPMC/Univ. Paris-Sud), Bat. 502, Rue du Belvedere, Campus Universitaire, 91405, Orsay Cedex, France
[b] Equipe de Dynamique des Fluides Geologiques, IPGP, 1 rue Jussieu, 75238 Paris Cedex 05, France
[c] Institute of Geophysics, ETH Zurich, Sonneggstrasse 6, CH-8092 Zurich, Switzerland

ARTICLE INFO

Article history:
Received 30 October 2012
Received in revised form 13 December 2012
Accepted 14 December 2012
Available online 31 December 2012

Keywords:
Numerical model
Thermal instabilities
Yield stress fluid
Carbopol
Herschel–Bulkley
Laboratory model

ABSTRACT

We present a three dimensional numerical study of thermal plumes, developing from a localized heat source in a yield stress and shear thinning fluid. We assume that the fluid viscosity follows a Herschel–Bulkley law with a low shear rate viscosity plateau. Comparison of the plume onset time and morphology observed in the numerical study and in laboratory experiments with Carbopol shows good agreement. An extensive parameter study allows us to identify two local non-dimensional parameters that determine whether a plume rises through the fluid. The first parameter is the Bingham number, Bi, which compares the yield stress to the viscous stress. The second parameter, the yield number Ψ, compares the stress induced by the buoyancy of an equivalent hot sphere to the yield stress. We find that a plume develops only if $\Psi > \Psi_c = 5 \pm 1.2$ and $Bi < Bi_c = 1$. As the plume rises it loses its buoyancy due to heat diffusion. So the upward progression of the plume halts as soon as $\Psi < \Psi_c$ or $Bi > 1$. Hot fluid continues to rise from the bottom of the tank but spreads under an unyielded, high viscosity region at the top of the box.

1. Introduction

Thermal convection and instabilities in yield stress fluids occur in many different fields, from engineering (food- or glass production, [1,2]) to geoscience (formation of dikes and diapirs in the lithosphere or convection in icy satellites, [3]). Despite its huge importance it is still not very well understood.

The theoretical difficulty in studying such systems is caused by an infinite viscosity as the shear rate approaches zero. Therefore an instability cannot grow from a conductive profile exposed to an infinitesimal perturbation [3–5]. Former studies on thermal instabilities in Rayleigh-Bénard convection in a yield stress fluid considered either a Bingham fluid [4], [6–10] or a purely shear thinning fluid [11,3]. However, fluids exhibiting a yield stress as well as shear thinning behaviour have not been studied extensively. Balmforth and Rust [5] investigated the stability of a weakly non-linear fluid, concluding that shear thinning favors an early onset of convection whereas a yield stress suppresses convection. The same authors tested their numerical predictions experimentally on Carbopol solutions in a Rayleigh-Bénard setup and found that fluids with a high Carbopol concentration, i.e. high yield stress, start to convect only if exposed to finite perturbations.

In a recent study Davaille et al. [12] investigated the development of a thermal plume in Carbopol rising from a localized heat source. The Carbopol rheology can be described by a Herschel–Bulkley model [13–16]. The experiments showed that thermal instabilities in a yield stress fluid behave very differently from those in Newtonian liquids.

A key parameter is the yield parameter, Y_0, which compares the thermally induced stresses to the yield stress and is therefore written as

$$Y_0 = \frac{\alpha \rho g P}{k \sigma_0}, \tag{1}$$

where α is the thermal expansivity, ρ is the density of the fluid at ambient temperature, g the acceleration due to gravity, P the thermal power supplied by the heat source, k the thermal conductivity and σ_0 the yield stress of the fluid. Depending on the yield parameter Y_0, the system evolves into one of three regimes, which are separated by two critical yield parameters, Y_{c1} and Y_{c2} (cf. [12]). For $Y_0 < Y_{c1}$ only elastic deformation occurs, while for $Y_{c1} < Y_0 < Y_{c2}$ a small cell slowly convects around the heater. Only a high yield parameter ($Y_0 > Y_{c2}$) allows the cell to evolve into a plume. This yield parameter is not to be mistaken for the yield number, Ψ, which is applicable to problems involving rising bubbles [17,18] or sinking spheres [19,20] in a yield stress fluid. The yield number is defined as

$$\Psi = \frac{\Delta \rho g 2 r_{eq}}{3 \sigma_0}. \tag{2}$$

* Corresponding author.
E-mail address: massmeyer@fast.u-psud.fr (A. Massmeyer).

0377-0257/$ - see front matter © 2012 Elsevier B.V. All rights reserved.
http://dx.doi.org/10.1016/j.jnnfm.2012.12.004

For bubbles and spheres, $\Delta\rho$ is the density difference between the object and the fluid and r_{eq} is the radius of the object. Bubbles or spheres move if $\Psi > \Psi_c = 6.85$ [17–20]. For a thermal instability, $\Delta\rho = \alpha\rho\Delta T$ and r_{eq} corresponds to the radius of a sphere with a volume equivalent to the volume of the hot pocket that forms around the heater [12]. Therefore for a thermal instability, although Y_0 is constant, Ψ evolves with time as the thermal boundary layer grows. It has been observed experimentally that the plume develops when $\Psi > 8.8 \pm 0.7$ [12].

The onset time t_0 of this plume, i.e. the time at which the plume starts to rise, depends on the yield parameter and increases with decreasing yield parameter. As Y_0 tends to Y_{c2}, the onset time goes to infinity. The shape of the thermal instability looks like a finger, unlike in a Newtonian fluid, where hot, less viscous plumes have a mushroom shape with a big head on a thin stem [21]. Most deformation is localized to the edges of the thermal anomaly and is orders of magnitude smaller within the thermal anomaly. This produces a pseudo-plug area on the plume axis. The evolution in time changes, depending on the rheological parameters of the fluid. For small consistencies, K_v, the plume can show an episodic behaviour whereas it rises continuously for high K_v.

In this study we use numerical simulations to investigate the extent to which a purely viscous fluid description, using a regularized Herschel–Bulkley model, is able to describe the evolution from the cell to the plume instability as well as the instability itself. We therefore systematically vary rheological and thermal parameters, as well as the applied thermal history of the heated patch. To confirm the adequacy of the model, we compare the morphology, the evolution in time and the dependence of the onset time on the yield parameter, Y_0, observed in our numerical model to laboratory results. This validation allows us to study a well defined parameter range, avoiding the uncertainties due to the difficulty in accurately measuring the rheological parameters in the laboratory. The advantage of numerical simulations is that they allow us to test how each rheological parameter, yield stress σ_0, consistency K_v and shear thinning exponent n, influence the evolution of the plume instability. We therefore varied these parameters systematically. Access to the full three dimensional fields allows us to find the key parameters that characterize the dynamics of the thermal instability.

2. The model

2.1. Governing equations

In this study, we consider the fluid to be incompressible and in the Boussinesq approximation. Furthermore we neglect viscous dissipation [22]. The fluid can be described by the simplified equations for conservation of mass

$$\nabla \cdot \underline{v} = 0 \tag{3}$$

momentum

$$\frac{D\underline{v}}{Dt} = -\frac{1}{\rho_0}\nabla p + \alpha\Delta T g\underline{e}_z + \nabla \cdot \underline{\underline{\sigma}} \tag{4}$$

and energy

$$\frac{DT}{Dt} = \kappa\nabla^2 T \tag{5}$$

where $\underline{v}$ is the velocity, $D/Dt = (\partial/\partial t + \underline{v} \cdot \nabla)$ the material derivative, ρ_0 is the density of the ambient fluid, p the pressure, α the thermal expansivity, ΔT the temperature difference between heater and ambient fluid, g the gravity acceleration, $\underline{\underline{\sigma}}$ the stress tensor, T the temperature and κ the thermal diffusivity.

2.2. The model rheology

The viscosity of Carbopol depends mainly on the shear rate, but also on temperature. The shear rate dependence can be described with a Herschel–Bulkley model [13,14,23], which implies infinite viscosity as the shear rate approaches zero. To avoid this difficulty in the numerical simulations we apply a viscosity truncation. Different models exist for a regularized Herschel–Bulkley model (e.g. [24,25]). We choose the model of de Souza Mendes and Dutra [26] due to its convenience for curve-fitting of the rheology measured in the laboratory. This allows for an easier comparison of simulations and experiments. The adequateness of this model to describe the flow of a Carbopol solution through an axi-symmetric expansion has been demonstrated in [27]. In a tensorial representation it is written as

$$\underline{\underline{\sigma}} = \left(1 - \exp\left(\frac{-\eta_0\dot{\gamma}}{\sigma_0}\right)\right)(\sigma_0 + K_{vT}\dot{\gamma}^n)\underline{\underline{\dot{\gamma}}}\dot{\gamma}^{-1}, \tag{6}$$

where the expression in the first bracket is the regularization term and the expression in the second bracket describes the Herschel–Bulkley model. The yield stress is given by σ_0, K_{vT} is the consistency, n the shear thinning exponent and $\dot{\gamma}$ the magnitude of the strain rate $\underline{\underline{\dot{\gamma}}}$. η_0 represents the upper viscosity cut-off and is chosen to be $\eta_0 = 10^8$ Pa s in all the calculations. In Section 3.2.1 we show that the dynamics of the plume is mostly independent of the cut-off value. To avoid too large viscosity contrasts, our numerical code uses an additional lower cut-off for the viscosity. However, we made sure that this lower value is never reached, so that it does not influence the dynamics. The value was set to $\eta_{min} = 0.01$ Pa s for $K_v \leqslant 0.1403$ Pa s^n and to $\eta_{min} = 0.1$ Pa s for the other cases.

The laboratory measurements showed that σ_0 and n do not depend on the temperature. However the consistency K_{vT} varies with temperature, following an Arrhenius-type law

$$K_{vT} = K_v A e^{B(T-273.15)}, \tag{7}$$

where $A = 1.6927$, $B = -0.0257$ K^{-1} and where K_v is the consistency at room temperature $T = 293.15$ K (for details see Appendix A).

2.3. The numerical model and boundary conditions

We solve the set of Eqs. (3)–(5) using a finite volume discretization on a staggered grid, implemented in the code StagYY. Code details and benchmarking for constant viscosity and temperature-dependent viscosity cases are described in detail in [28] (pp. 286–290 for benchmarking results) and more briefly in [28–30]. For the diffusive term, second order finite differences are used, and a second order upwind scheme is used for the advective terms. The convergence criterion is met, if the normalized residuals of the momentum and continuity equations is smaller than 10^{-2}.

Even though most of the characteristics observed for the plume in the laboratory are axi-symmetric, the tank in the laboratory is not. We need to use straight walls in order to avoid optical distortions during the visualization. To ensure the same boundary conditions as in the laboratory, we use a three-dimensional Cartesian box (Fig. 1). The box is 20 cm long and wide and 40 cm high with a resolution of $64 \times 64 \times 128$ grid points. We verified that higher resolutions give the same results. The boundary conditions are described by a no-slip and zero-flux condition for the bottom and sidewalls. The top boundary is free-slip and kept at ambient temperature. To compare with the experiments, for which the heating power is constant, we prescribed the temperature history of the heater measured in the laboratory experiments. We calculate the thermal power P, defined as the surface integral of the heat-flux

$$P = \int Q dA, \tag{8}$$

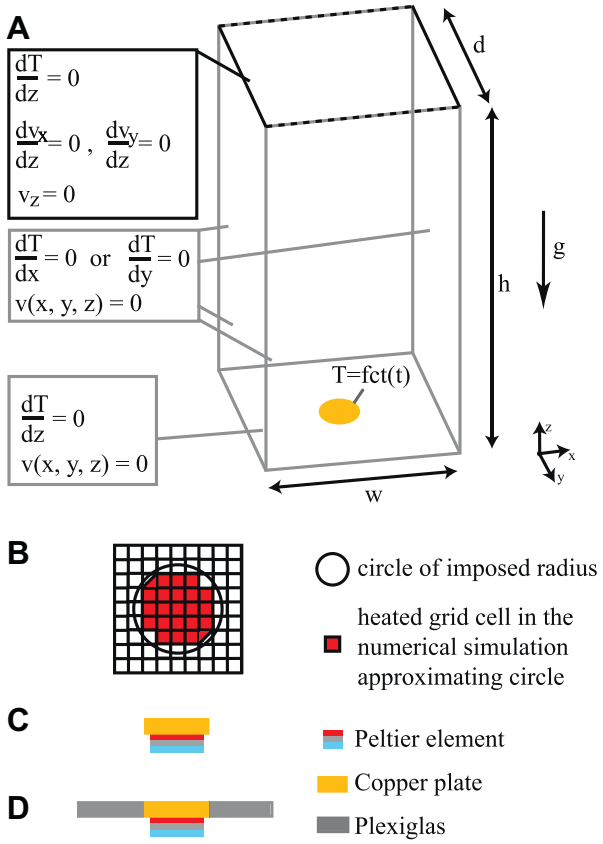

Fig. 1. (A) Schematic illustration of the numerical domain. The calculations are run in a box of $w \times d \times h = 20\text{ cm} \times 20\text{ cm} \times 40\text{ cm}$ with a resolution of $n_x \times n_y \times n_z = 64 \times 64 \times 128$. Top boundary: free-slip, and kept at ambient temperature T_0, side walls and bottom plate: rigid with zero heat flux. Patch in the center of the bottom of the box follows a prescribed temperature evolution. (B) schematic of the approximation of the circular heated patch in the numerical simulation. While in the simulations the heated patch is inside the bottom boundary, in the laboratory experiments it is either; (C) bottom mounted [12] or (D) flush mounted by embedding the copper disk into a Plexiglas plate.

which is needed for comparison with the laboratory experiments (e.g. [12]), where Q denotes the heat flux and dA the surface through which the heat flux is measured. For the numerical simulations the thermal power is constant within 5% through time, prior to the onset, and increases when the plume rises, as the heat flux is increased. We generally refer to the minimum value, when dealing with the thermal power P.

Due to the numerical grid (Fig. 1B), the heated surface is smaller than the surface of an equivalent circle with the same radius. With the resolution $64 \times 64 \times 128$ and a radius of $r = 1.25$ cm this implies a heated surface of 3.93 cm^2 instead of the surface of the circle 4.91 cm^2. The smaller surface of the disk results in a smaller heat flux and therefore a smaller thermal power P. However, Davaille et al. [12] showed that the system depends strongly on the yield parameter Y_0 (Eq. (1)), therefore a smaller P can be adjusted with a higher σ_0 or α.

2.4. The laboratory experiments

The setup of the laboratory experiments and the procedure by which the fluid is prepared is described in [12]. The heater consists of a Peltier element underneath a copper disk. In the first set of experiments Davaille et al. [12] the heater was placed on top of the tank bottom (Fig. 1C). In addition, we performed a series of experiments with a flush mounted heater (Fig. 1D), in order to mimic the boundary conditions in the numerical simulations. Additionally in the new series we also studied the influence of higher fluid depths, up to $h = 39.2$ cm.

3. Validation of the purely viscous description

3.1. Input and output parameters

In this study we systematically vary the thermal and rheological parameters (values listed in Table 1) to evaluate the effect on the dynamics of the plume. Here we will briefly demonstrate the general evolution of a plume and how we evaluate the diagnostic parameters (listed in Table 1).

Fig. 2 shows the typical evolution of the thermal instability. Upon heating, a hot pocket of fluid forms by heat conduction around the heater. Very slow motions are recorded in this hot pocket. After approximately 1 h, a plume develops. The shape of the isotherm (Fig. 2A) resembles a finger.

From Eq. (6), we can calculate an effective viscosity

$$\eta = \underline{\underline{\sigma}}\dot{\gamma}^{-1} = \left(1 - exp\left(\frac{-\eta_0\dot{\gamma}}{\sigma_0}\right)\right)(\sigma_0 + K_v\dot{\gamma}^n)\dot{\gamma}^{-1}. \quad (9)$$

Fig. 2B shows that there remains an unyielded region (i.e. where the viscosity value remains at the cut-off value) at the top of the box during the whole simulation. This means that the plume has stopped rising. In the systematic study below, we shall use two diagnostic variables to characterize the plume evolution: the onset time t_0 (Fig. 2C), and the height where the plume stops h_y (Fig. 2D).

- *Onset time*: Lower viscosity regions form already at an early stage of the plume (Fig. 2B and C a)), due to a slowly convecting cell around the heater. The spatiotemporal evolution (Fig. 2C) shows that at $t = 62.33$ min (Fig. 2b)) this cell grows very fast. The time when the small cell evolves into a plume is referred to as the onset time t_0. Several methods to determine the onset time all give similar results within an error of 3% [12]. We will show how the transition from the cell to the plume takes place and provide a precise criterion for the determination of the onset time in Section 5.1.
- Height where the plume stops: The spatiotemporal evolution of the viscosity on the plume axis (Fig. 2C) shows that even after the onset of the plume, high viscosity regions persist at the top of the box. This means that not the whole fluid is convecting, but only a part of it. To define the height where the plume stops, we plot a profile of the viscosity on the plume axis (Fig. 2D). The viscosity shows a local minimum at the head of the plume. This local viscosity minimum corresponds to the point where the radial derivative of the radial velocity (dv_r/dr) becomes maximum. Hence, it marks the location of a stagnation point in the moving plume reference frame, and therefore the position of the top of the plume head [21]. So, we define the maximum height that a plume reaches, or height where the plume stops, h_y, as the maximum height of the stagnation point. This height only varies very gently through time, once a quasi stationary state is reached. This is assured for all calculations 50 min after the onset of the plume, when the height changes become negligibly small (<1 mm over 50 min). We always measure this height at the end of each calculation.

3.2. Influence of the model simplifications

3.2.1. Effects of the viscosity cut-off η_0

We tested the influence of different η_0 on the plume dynamics, $\eta_0 = [10^8, 10^{10}, 10^{12}]$ Pa s. The choice of η_0 neither affects the onset

Table 1
Shear thinning exponent n, consistency K_v, yield stress σ_0, thermal expansivity α, onset time t_0, the thermal power P, height reached by viscosity minimum at plume head at for all numerical simulations h_y and respective yield parameter Y_0.

#	σ_0 (Pa)	K_v (Pa s^n)	n (–)	α (10^{-4}/K)	t_0 (min)	P (W)	h_y (cm)	Y_0 (–)	#	σ_0 (Pa)	K_v (Pa s^n)	n (–)	α (10^{-4}/K)	t_0 (min)	P (W)	h_y (cm)	Y_0 (–)
1	0.0100	0.140	0.58	6.00	1.3550	1.709	–	2666.26	29	0.0630	1.403	0.58	4.78	77.2340	1.157	26.85	228.26
2	0.0100	1.000	0.58	4.78	2.3712	1.539	40.00	1912.83	30	0.0650	1.000	0.58	4.78	82.6539	1.16	30.63	221.81
3	0.0100	1.000	0.58	4.78	3.0487	1.215	40.00	1510.13	31	0.0650	1.000	0.50	4.78	108.3985	1.148	28.92	219.51
4	0.0100	1.403	0.58	6.00	1.3550	1.552	40.00	2421.31	32	0.0650	1.000	0.70	4.78	67.7491	1.18	37.22	225.64
5	0.0100	1.403	0.90	6.00	1.3550	1.682	40.00	2624.13	33	0.0650	1.403	0.58	4.78	90.7838	1.157	28.23	221.24
6	0.0200	1.000	0.58	4.78	5.7587	1.463	40.00	909.18	34	0.0650	1.403	0.50	4.78	131.4332	1.139	27.20	217.80
7	0.0200	1.403	0.58	4.78	5.4199	1.429	40.00	888.05	35	0.0650	1.403	0.70	4.78	71.8140	1.172	31.63	224.11
8	0.0200	1.403	0.58	6.00	4.4037	1.481	40.00	1155.28	36	0.0650	2.000	0.58	4.78	105.6886	1.15	26.16	219.90
9	0.0250	1.403	0.58	4.78	6.7749	1.449	31.63	720.39	37	0.0650	2.000	0.50	4.78	181.5675	1.122	26.16	214.54
10	0.0300	1.403	0.58	4.78	10.1624	1.380	27.85	571.74	38	0.0650	2.000	0.70	4.78	75.8790	1.165	28.92	222.77
11	0.0350	1.403	0.58	4.78	13.5498	1.341	24.95	476.21	39	0.0670	0.140	0.58	4.78	82.6539	1.158	40.00	214.82
12	0.0400	0.140	0.58	4.78	12.8723	1.346	–	418.28	40	0.0670	1.000	0.58	4.78	98.9137	1.148	32.62	212.96
13	0.0400	0.140	0.58	6.00	8.1299	1.426	–	556.18	41	0.0670	1.403	0.90	6.00	81.2989	1.156	40.00	269.18
14	0.0400	1.000	0.58	4.78	16.9373	1.317	23.9	409.255	42	0.0670	1.403	0.58	6.00	37.2620	1.227	23.5	285.71
15	0.0400	1.403	0.58	4.78	16.9373	1.308	22.67	406.43	43	0.0670	1.403	0.58	4.78	108.3985	1.145	29.61	212.41
16	0.0400	1.403	0.58	6.00	10.8399	1.367	27.2	533.17	44	0.0670	2.000	0.58	4.78	126.0133	1.144	27.54	212.22
17	0.0400	1.403	0.90	4.78	8.1299	1.427	40.00	443.41	45	0.0670	14.000	0.58	4.78	1400[a]	1.025	0	190.15
18	0.0500	1.000	0.58	4.78	30.4871	1.28	23.37	318.18	46	0.0675	1.403	0.58	4.78	113.8185	1.156	30.29	212.86
19	0.0500	1.403	0.58	4.78	33.8745	1.263	21.8	313.96	47	0.0680	1.403	0.58	4.78	120.5934	1.140	30.96	208.37
20	0.0600	1.000	0.58	4.78	55.5542	1.196	27.20	247.75	48	0.0700	1.000	0.58	4.78	131.4332	1.157	36.00	205.43
21	0.0600	1.000	0.50	4.78	73.1690	1.183	25.81	245.06	49	0.0700	1.000	0.50	4.78	170.7277	1.123	33.59	199.40
22	0.0600	1.000	0.70	4.78	46.0694	1.215	30.29	251.69	50	0.0700	1.000	0.70	4.78	113.8185	1.215	40.00	215.73
23	0.0600	1.403	0.58	4.78	62.3292	1.183	25.11	245.06	51	0.0700	1.403	0.58	4.78	146.3380	1.14	32.95	202.42
24	0.0600	1.403	0.50	4.78	89.4288	1.163	24.07	240.92	52	0.0700	1.403	0.50	4.78	222.0000	1.111	31.63	197.27
25	0.0600	1.403	0.70	4.78	48.7793	1.198	27.89	248.17	53	0.0700	1.403	0.70	4.78	117.8834	1.137	40.00	201.88
26	0.0600	2.000	0.58	4.78	73.1690	1.173	23.37	242.99	54	0.0700	2.000	0.58	4.78	166.6627	1.138	30.29	202.06
27	0.0600	2.000	0.50	4.78	108.3985	1.146	23.37	237.39	55	0.0700	2.000	0.50	4.78	319.7757	1.103	30.63	195.85
28	0.0600	2.000	0.70	4.78	51.4893	1.195	26.16	247.55	56	0.0700	2.000	0.70	4.78	121.9483	1.145	34.22	203.30

[a] Plume develops even after that time.

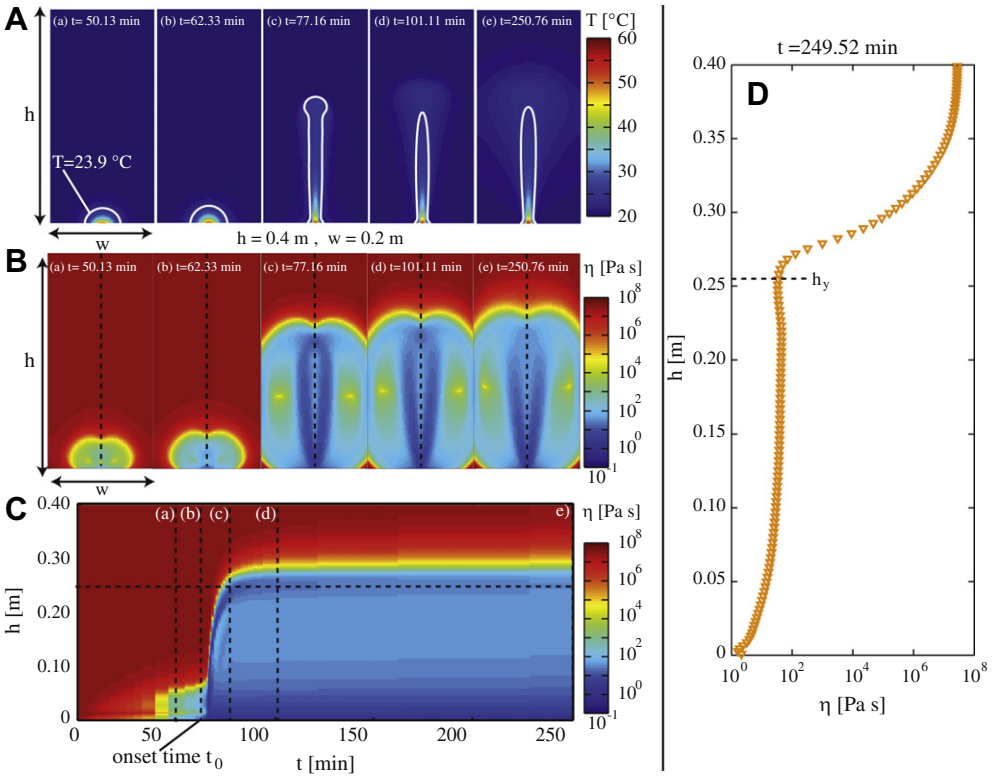

Fig. 2. Definition of output parameters. (A) snapshots of the temperature field in the axis plane for different time steps marked in C. White lines mark the isotherm at T = 23.9 °C. (B) snapshots of the viscosity field on the plane through the plume axis. (C) spatiotemporal evolution of a vertical line on the plume axis for the viscosity, vertical dotted lines in B and C correspond to each other. (D) viscosity profile at t = 249.52 min, h_y marks the height where the plume stops, corresponding to local minimum in the viscosity, which marks stagnation point.

time, nor the dynamic behaviour (Fig. 3A). The viscosity profile inside the plume remains the same (Fig. 3B), and only the unyielded structure above the plume ($h > h_y$) is influenced by the cut-off value. However the height where the plume stops, h_y, does not change for different cut-off values (see close up Fig. 3). This shows that the regularization has no significant influence on the plume's behaviour. Given this result, all simulations were run with the same viscosity cut-off value of $\eta_0 = 10^8$ Pa s.

3.2.2. Dependence on the thermal history

The laboratory experiments [12] have a constant heating power, which leads to a temperature drop in the copper plate when heat is suddenly taken away by the plume lift off (Fig. 4A i) solid blue line). However, in the present paper we intend to vary the rheological parameters. An increase in the yield stress will then lead to an increase in the onset time. If the onset time lies beyond the onset time of the laboratory experiments, a temperature drop in the heated patch would influence (delay or suppress) the onset time or might affect the dynamics of a plume that starts before the laboratory plume. Therefore we generalize the heating history by smooth prolongation of the thermal history curve prior to the onset (cf. Fig. 4A i) dashed orange line). In the case of the real temperature history, the unyielded region is slightly larger, i.e. h_y is smaller, than for the generalized heating. As the supply of heat drops slightly in the laboratory case, the plume is less buoyant and rises less high. However, the difference is rather small, 3% of the absolute value (cf. cross section at 250 min Fig. 4B). Keeping this in mind, we will use in most of the runs the simplified heating history as shown by the dashed orange line in Fig. 4A i).

3.3. Comparison with laboratory experiments

The uncertainties of the laboratory experiments, e.g. an error of 30% [12] on the yield stress, make it difficult to match the exact conditions and to reproduce a series of experiments. As we will show in detail later, the system is very sensitive to small changes, not only in yield stress, but also in shear thinning exponent or in consistency. However, we will show here that the basic characteristics of laboratory experiments, e.g. a finger-like instability and a strong dependence of the onset time on the yield parameter Y_0 [12], are well captured by our numerical model. Furthermore, in a new set of laboratory experiments with a larger fluid height, we observe the persistance of unyielded regions even after the plume is established. Davaille et al. [12] had not been able to observe this phenomenon, due to the smaller fluid height. This will allow us to examine in more detail how each rheological property affects the dynamics of the system.

3.3.1. Onset and evolution

Fig. 5 shows the dependence of the onset time on the yield parameter Y_0, for the numerical simulations, the flush mounted experiments and the bottom mounted experiments [12]. The onset-time of the plume strongly depends on the yield parameter Y_0. The numerical simulations show a good agreement with the results obtained with the modified setup, where the heating is flush mounted. The critical value for the flush mounted experiments and for the numerical simulations is $Y_c \approx 165 \pm 25$. The dash-dotted line in Fig. 5 marks the lower limit at $Y_0 = 140$, and the error can be explained with the uncertainties in the laboratory measurements (10% on the thermal power P and 30% on the yield stress σ_0). However, the critical value for the flush mounted experiments is well below the value for the bottom mounted heating determined by [12] of $Y_{c2} = 260$. We attribute this discrepancy to the different heater shapes, which will change the local stress distribution. The plot suggests that n and K_v also influence the onset time, however this will be discussed later. Globally, the plot shows that the onset time approaches two asymptotical values, depending on the yield stress. For low yield parameter, i.e. when the yield stress is important compared to the thermally induced stresses, the onset time is increasing rapidly with decreasing Y_0. On the other end, for high

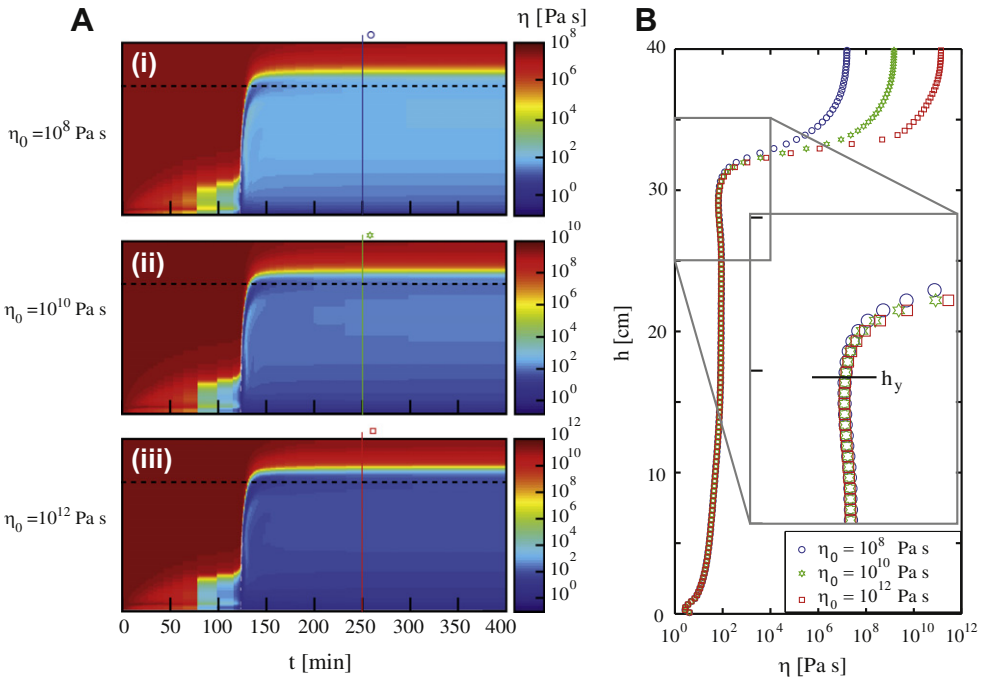

Fig. 3. (A) Spatiotemporal evolution of the viscosity at the plume axis for three different viscosity cut-offs η_0. (B) vertical viscosity profile at $t = 250$ min for the different cut-off values $\eta_0 = 10^8$ Pa s (blue circles), $\eta_0 = 10^{10}$ Pa s (green stars), $\eta_0 = 10^{12}$ Pa s (red squares). The height h_y in B is marked in A by the horizontal black dashed lines, corresponding to a local minimum viscosity. (For interpretation of the references to colour in this figure legend, the reader is referred to the web version of this article.)

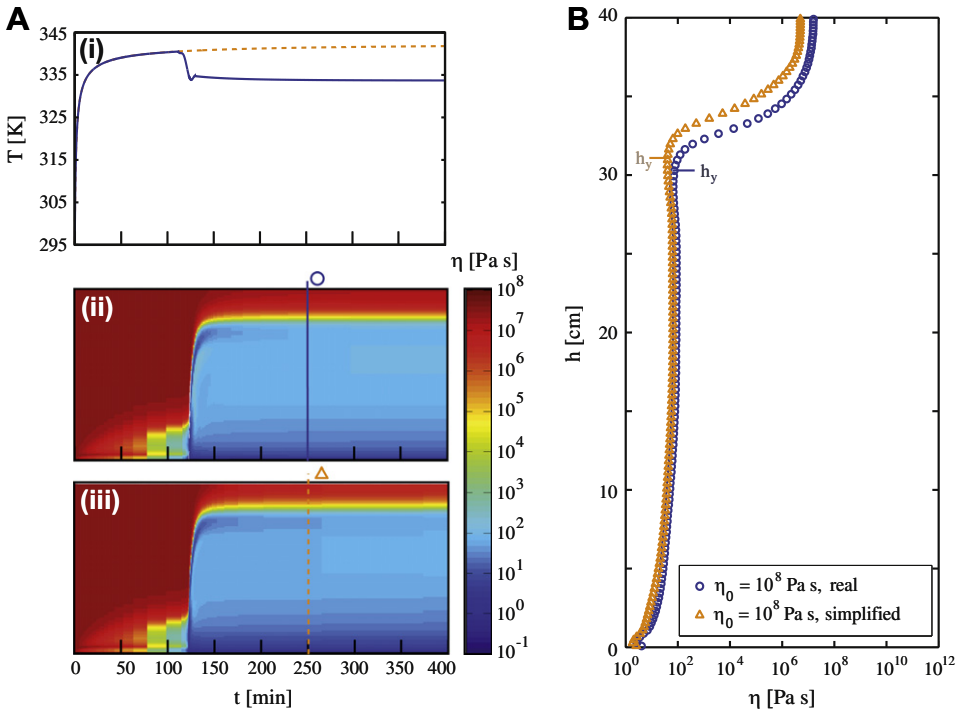

Fig. 4. Effect of real (A i) solid blue) and generalized (A i) dashed orange) thermal history on the evolution of the plume. Spatiotemporal evolution for the viscosity of a vertical line at the plume axis (ii) laboratory and (iii) generalized temperature history of the heated patch. B: cross section of (A ii) (blue circles) and (A iii) (orange triangles) at t = 250 min. (For interpretation of the references to colour in this figure legend, the reader is referred to the web version of this article.)

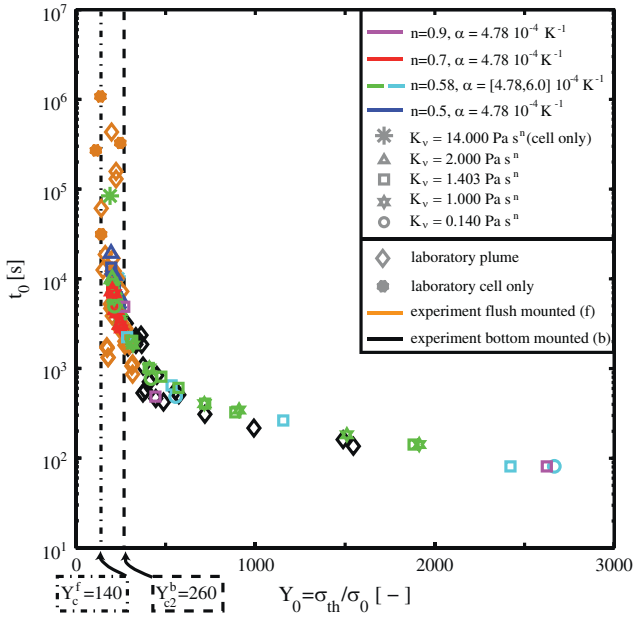

Fig. 5. Onset time dependence on the non-dimensional yield parameter Y_0 which compares the buoyancy induced thermal stress to the yield stress. Diamonds indicate plumes obtained from laboratory experiments including those of [12] (black) and those obtained with the flush mounted heater (orange). Orange octagons: laboratory experiments that exhibit a cell only until the depicted time. All other symbols: Numerical simulations, colours indicate different n, while different symbols indicate different K_v. (For interpretation of the references to colour in this figure legend, the reader is referred to the web version of this article.)

yield parameter, i.e. low yield stresses, the onset time approaches a finite limit. This is to be expected as the system turns towards the purely shear thinning or Newtonian case.

In Fig. 6 the typical spatiotemporal evolutions of a plume for both laboratory and numerical simulations, are compared. Fig. 6 A presents the time evolution of the heated patch for experiment (black) and simulation (grey), in the case where we used the real temperature history. Fig. 6C shows a typical snapshot of the plume in the laboratory experiments. The white broad lines outlined in colour are isotherms (blue dash dotted: 23.9 °C, yellow dotted: 31.1 °C, red dashed: 39.9 °C) and thin white lines correspond to particle trajectories. Therefore a horizontal line indicates a particle at rest and white streaks upwards and towards the right are particles moving upwards along the axis. Fig. 6D shows the vertical viscosity profile on the plume axis for the numerical simulations where the viscosity increases from dark blue to dark red. Black lines indicate the position of the same isotherms as visualized in the laboratory, where temperature is increasing from inside (bottom) to outside (top).

The thermal power in the laboratory is $P = 1.85 \pm 0.185$ W, the yield stress is determined to be $\sigma_0 = 0.09 \pm 0.015$ Pa, the consistency $K_v = 1.403 \pm 0.2$ Pa s^n and the shear thinning exponent is determined to be $n = 0.58 \pm 0.01$. The measurements have been done using a Physica MCR501-rheometer (Anton Paar, www.anton-paar.com) with a coaxial cylinder geometry (CC27).

We find a good agreement of the onset-time derived from the numerical simulation and the laboratory experiment (t_0 = 119.9 min in the laboratory, t_0 = 120.59 min in the simulations, t = 120 min indicated by the green dashed line) with the parameter combination $P = 1.14$ W, $\sigma_0 = 0.068$ Pa, $K_v = 1.403$ Pa s^n and $n = 0.58$. The thermal properties are the same with small errors on the values for the experiments. The thermal expansivity is $\alpha = 4.78 \pm 0.01$ K^{-1} and the thermal conductivity is $k = 0.435 \pm 0.02$ W/m K. Therefore we can calculate the yield parameter for the laboratory experiments $Y_0 = 266.86 \pm 71.09$ and for the numerical simulations $Y_0 = 208.36$. The value for the simulations is well within the error range of the laboratory experiments, explaining the good agreement of the onset times.

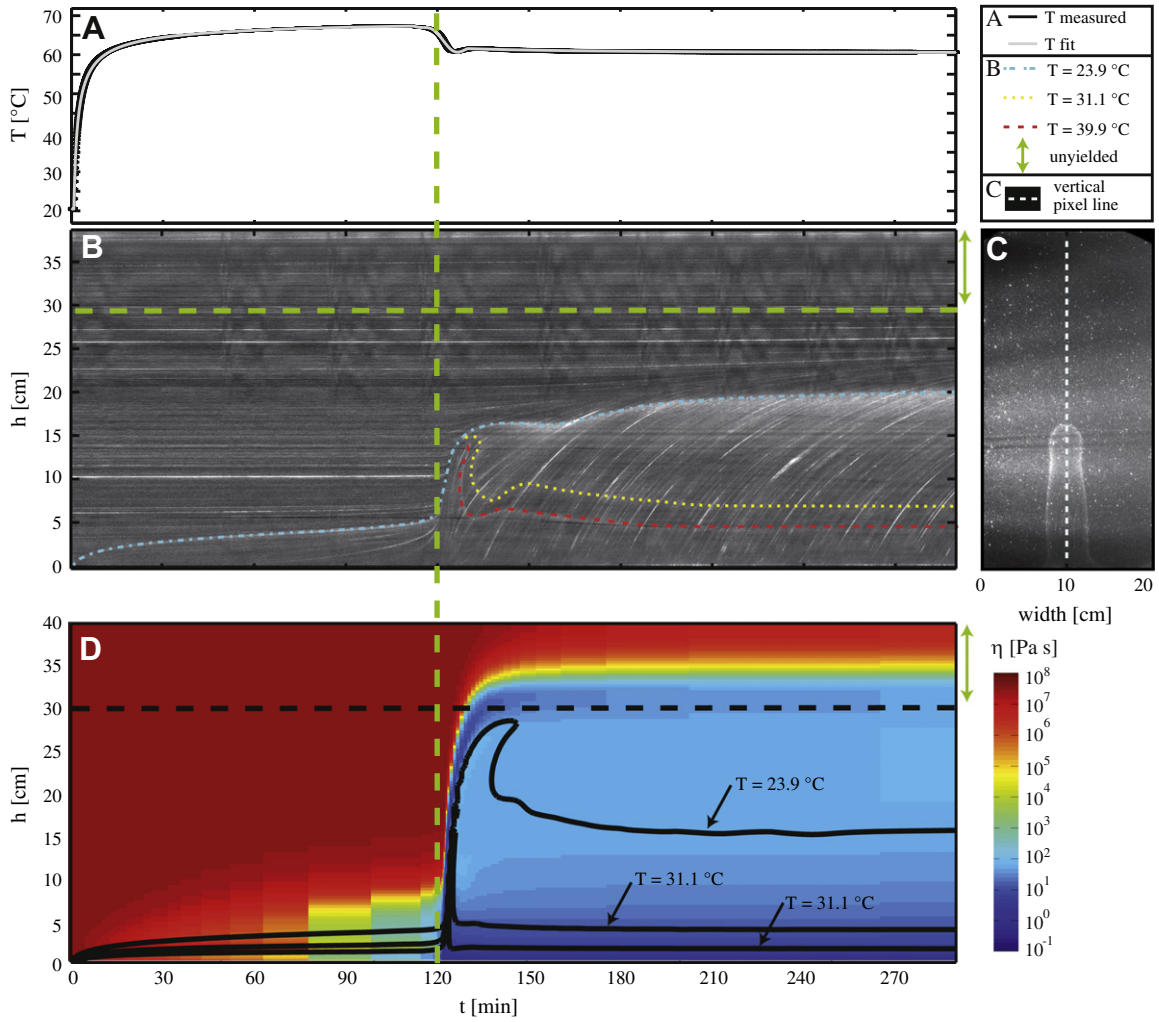

Fig. 6. (A) Evolution of the heating for the laboratory experiments (black line) and the numerical simulation (grey line) through time. (B) Spatiotemporal evolution of a vertical pixel line (vertical white dashed line in C) through time. White lines show particles, coloured lines highlight the isotherms at 23.9 °C (blue dash dotted), 31.1 °C (yellow dotted) and 39.9 °C (red dashed). (C) Snapshot from a laboratory experiment at t = 146 min, the white dashed line marks plume axis. (D) Spatiotemporal evolution of the viscosity at the plume axis (background colour) and isotherms (black lines). The vertical green dashed line indicates the onset time, which is about the same (laboratory experiment: t_0 = 119.9 min, numerical simulation t_0 = 120.59 min) for simulation and experiment. The horizontal green line marks the unyielded region for the laboratory experiment; the width of this region for experiment and simulation is given by the green arrows. (For interpretation of the references to colour in this figure legend, the reader is referred to the web version of this article.)

However, a match of both onset times does not necessarily imply an identical behaviour of the developping instability (Fig. 6). This is most evident for the isotherms, which, for the simulations, propagate much higher at the onset than in the experiment. There are also similarities: the upper part of the box remains unyielded through time, as indicated by the green arrows. In the experiments this can be seen by following the particles in the upper part of the box. They describe a horizontal line, i.e. the particles are not moving (Fig. 6B). In the numerical simulations the very high viscosity (dark red regions in the figure) indicates that shear rate vanishes and that the fluid is not moving. The maximum shear rate at the plume head is represented by the low viscosity in this region as highlighted by the horizontal black dashed line. Above this line viscosity increases rapidly.

3.3.2. The plume morphology

Fig. 7 shows that small shear rates are already present before the plume evolves, while the isotherms (black lines) still have a circular shape. A small cell is convecting around the heater and as the shear rate increases, this cell evolves into a plume. This plume then exhibits locally very strong deformation, which is localized on the edges of the thermal anomaly. The deformation is much weaker inside (difference of two orders of magnitude). Above the plume, the fluid exhibits unyielded regions. The inner structure of the thermal anomaly develops as a plume with a small head (A ii) and B iii)) whereas the outer isotherm looks more like a finger. Once the small head is lost, only the stem remains midway in the tank.

The instability in the simulations develops just like the instability in the experiments. The dependence of the onset time on the yield parameter is the same as in the laboratory experiments. The thermal anomaly looks like a finger and the instability exhibits strong deformation at the edges of the thermal anomaly and a pseudo-plug flow inside the thermal instability, as observed in the laboratory. Therefore we conclude that the purely viscous regularized Herschel–Bulkley model is a sufficient description of the fluid and suitable for studying numerically the development of thermal plumes in Herschel–Bulkley fluids like Carbopol.

4. Effects of rheological parameters on the dynamics

The laboratory experiments of Davaille et al. [12] show a strong dependence of the onset time and evolution of the plume on the

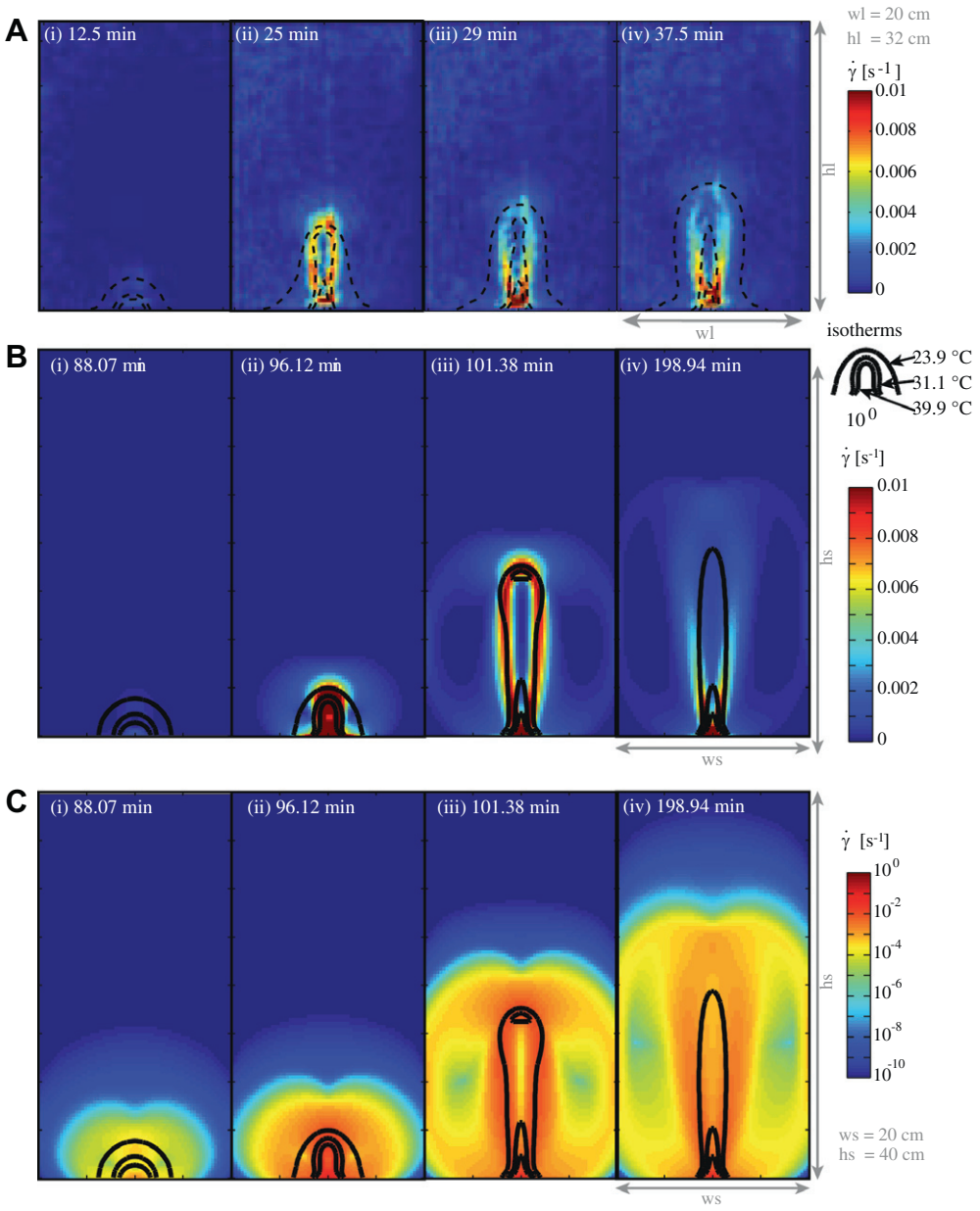

Fig. 7. Morphology of the deformation (background colour) and the temperature field as indicated by the isotherms (black lines, temperature increases from the inside to the outside, isotherms at 39.9 °C, 31.1 °C and 23.9 °C). (A) Laboratory experiment. (B) Numerical simulation. A and B are shown for the same shear rate range (colour bar at the side). (C) Numerical simulation for a larger shear rate. (For interpretation of the references to colour in this figure legend, the reader is referred to the web version of this article.)

yield stress. A closer look at different flow curves (Fig. 8) reveals that a change of the shear thinning exponent (Fig. 8A) and/or the consistency (Fig. 8B) might also affect the system, as those changes affect the effective viscosity. The flattening of the viscosity curve (Fig. 8A and B i)) and the deviation from the stress plateau (Fig. 8A and B ii)) for shear rates $\dot{\gamma} < 10^{-8}$ s^{-1} are due to the viscosity cut-off η_0. The uncertainties on the determination of the rheological parameter make it difficult to study the effect of small changes in the laboratory. We therefore examine numerically how small changes for all rheological parameters (σ_0, K_v and n) influence the development of the plume.

In order to investigate the effect of the yield stress on the plume's dynamics we varied σ_0 between 0.01 Pa and 0.07 Pa for constant K_v = 1.403 Pa s^n and n = 0.58. With increasing yield stress (Fig. 9A) from (i) σ_0 = 0.035 Pa over (ii) σ_0 = 0.04 Pa to (iii) σ_0 = 0.06 Pa, the onset time increases, as the yield parameter diminishes. At a given power P it then becomes increasingly difficult for the hot pocket to overcome the yield stress and to penetrate the surrounding fluid. Increasing the yield stress from σ_0 = 0.035 Pa to σ_0 = 0.04 Pa induces a decrease of h_y. As the plume cools down on its way up by heat diffusion (cf. Fig. 10 isotherms), its thermal buoyancy decreases until it cannot anymore overcome the yield stress. h_y should therefore depend on the initial buoyancy and the yield stress. At a given P, we expect h_y to decrease with increasing σ_0, as is observed. However, a further increase of the yield stress yields again a higher h_y, which may appear surprising at first. Yet this could be explained by the strong increase of the onset time when approaching the critical yield parameter, which allows the plume to accumulate more buoyancy before rising.

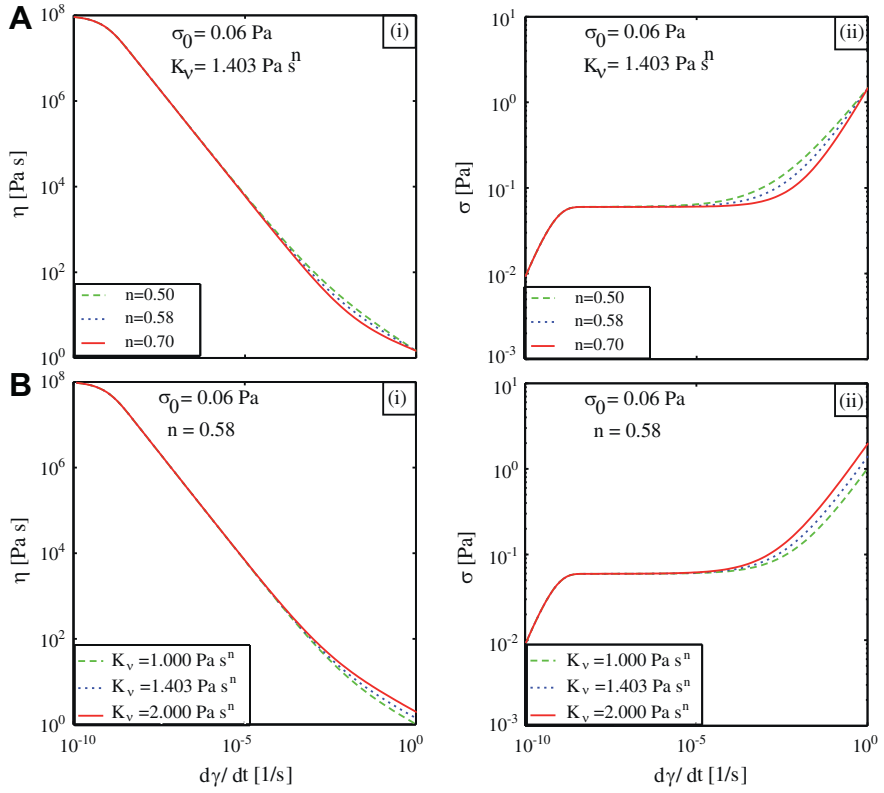

Fig. 8. Flow curves for different parameter combinations, (i) viscosity versus shear rate and (ii) stress versus shear rate. (A) Constant $\sigma_0 = 0.06$ Pa and $K_v = 1.403$ Pa s^n and varying shear thinning exponent $n = [0.50, 0.58, 0.70]$. (B) Constant $\sigma_0 = 0.06$ Pa and $n = 0.58$ and varying consistency $K_v = [1.000, 1.403, 2.000]$ Pa s^n.

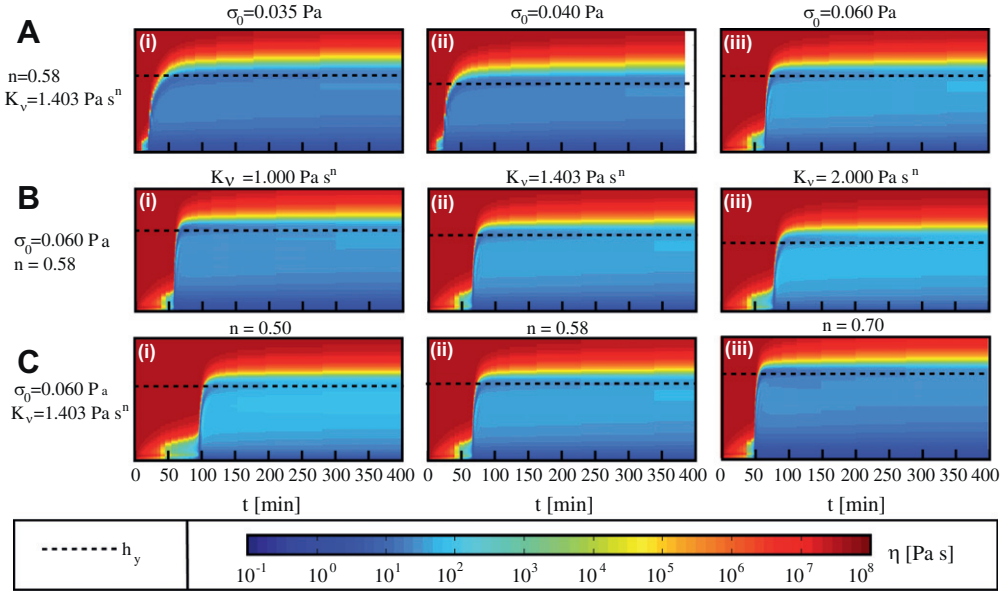

Fig. 9. Spatiotemporal evolution for the viscosity of a vertical line at the plume axis through time for (A) increasing yield stress at constant $K_v = 1.403$ Pa s^n and $n = 0.50$ (B) increasing consistency at constant $\sigma_0 = 0.060$ Pa and $n = 0.58$ and (C) increasing shear thinning exponent at constant $\sigma_0 = 0.060$ Pa and $K_v = 1.403$ Pa s^n. Horizontal black dashed lines mark h_y.

The increase of height h_y with increasing yield stress can also be observed in the laboratory experiments. In terms of the yield parameter Y_0, an increase in the yield stress is comparable to a decrease of the thermal power P. Fig. 10 shows the spatiotemporal evolution of the pixel line on the plume axis for two laboratory experiments with the same fluid, but with different thermal power P. The experiments show that, like in the numerical simulation, a decrease in Y_0 (obtained by decreasing P in the experiments and increasing σ_0 in the simulations) leads to an increase of h_y.

We furthermore tested numerically that we obtain the same behaviour by applying a constant temperature. So, whatever the details of the heater history are (constant power in the laboratory

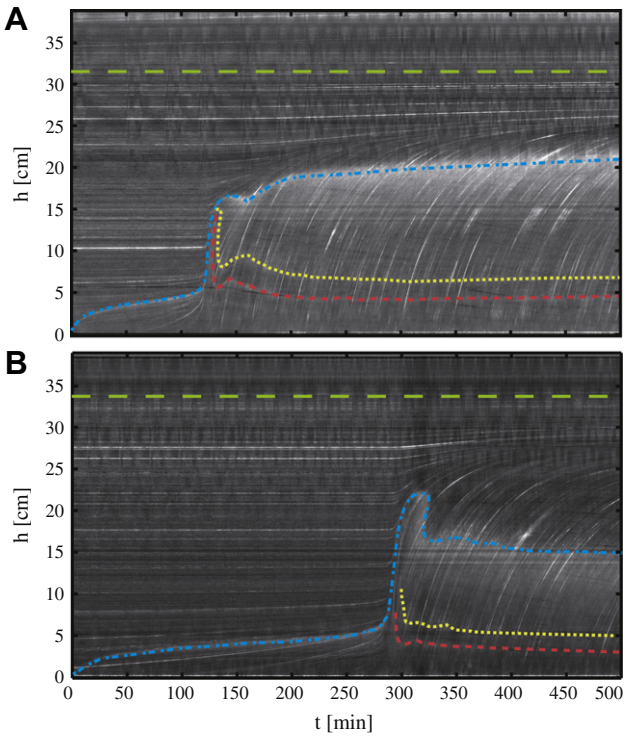

Fig. 10. Spatiotemporal evolution of a vertical pixel-line at the plume axis for two laboratory experiments in the same fluid, with different thermal power applied. (A) $P = 1.85$ W. (B) $P = 1.50$ W. Coloured lines highlight isotherms, colour and linestyle convention as in Fig. 6B. Green lines indicate the transition to unyielded region.

experiments or simplified temperature history in the simulations or constant temperature) h_y is not a monotonous function of Y_0, but with increasing Y_0, h_y first decreases and then increases again.

The effect of the increase of the consistency is depicted in Fig. 9B and increases from (i) $K_v = 1.0$ Pa s^n to (iii) $K_v = 2.0$ Pa s^n at $\sigma_0 = 0.06$ Pa and $n = 0.58$. The flow curve for the viscosity (Fig. 8B i)) shows that a fluid with a high consistency exhibits higher viscosities at constant shear rate. As a result, we observe that the onset time changes only slightly (compared to the effect of a change in the yield stress), as the consistency increases. On the other hand h_y decreases with increasing K_v by ≈15% from $K_v = 1.0$ Pa s^n to $K_v = 2.0$ Pa s^n. Inside the instability the viscosity increases with increasing K_v. With constant $\sigma_0 = 0.06$ Pa and $K_v = 1.403$ Pa s^n an increase of the shear thinning exponent induces lower viscosities for a given shear rate, Fig. 8A i). Therefore, the onset time decreases (Fig. 9C) when n increases from (i) $n = 0.5$ to (iii) $n = 0.7$. Furthermore this decrease in the effective viscosity also results in higher h_y.

5. Discussion

5.1. The onset of the plume

As we saw in the previous section, the onset time does not only depend on the yield parameter, but also on the consistency and the shear thinning exponent. A parameter comparing the yield stress to the viscous stresses is the Bingham number, which is for a Herschel–Bulkley fluid defined as

$$Bi = \frac{\sigma_0}{K_v \dot{\gamma}^n}. \tag{10}$$

We calculate this parameter using the maximum shear rate at each time step and then track the evolution of Bi (Fig. 11A). Fig. 11B shows the evolution of the viscosity on the plume axis. A comparison of both plots shows that the Bingham number value becomes $Bi = 1$ right prior to the take off of the plume. We can furthermore compare this to the evolution of the temperature field; Fig. 11C shows the temporal evolution of a vertical pixel line at the plume axis and Fig. 11D a horizontal pixel-line cutting the thermal boundary layer through the plume axis. The grey dotted line indicates the onset time as determined in the laboratory experiments [12], where the necking of the isotherms as seen in Fig. 11D has been used as a criterion for the onset. The state at which $Bi = 1$ occurs slightly before the onset as determined by the deformation of the isotherms in (Fig. 11D). However, when we plot the onset time as determined from the isotherms versus the onset time determined by the criterion $Bi = 1$ for different rheologies (Fig. 13) the data collapse on a straight line of slope one. Therefore, the Bingham number criterion is suitable to determine the onset time. Additionally, this method provides a more accurate determination of the onset time, since the other methods depend on the choice of the isotherm (cf. Fig. 11D: the inner (red) isotherm deforms earlier than the outer (blue) isotherm).

$Bi = 1$ at onset gives a characteristic scale for the shear rate that has to be overcome to generate a plume. This critical shear rate is then written as

$$\dot{\gamma}_{cr} = \left(\frac{\sigma_0}{K_v}\right)^{1/n}. \tag{11}$$

This further implies that at onset the local stresses fulfill the following criterion

$$\sigma = \sigma_0 + K_v \left(\left(\frac{\sigma_0}{K_v}\right)^{1/n}\right)^n = 2\sigma_0. \tag{12}$$

The experiments of Davaille et al. [12] indicate that the critical yield number Ψ as defined for bubbles to rise [17,18]) or spheres to sink [19,20] in a yield stress fluid is also applicable for the onset of the plume. The data range accessible from the simulations provides a much cleaner way to determine this parameter, than by the laboratory experiments. Similar to [12] we determine the volume of the fluid with a temperature excess $0.1\Delta T$ at the onset, where ΔT is the temperature difference between the heated patch and the ambient fluid. We then calculate the equivalent radius of a sphere with the same volume r_{eq} and determine its mean buoyancy, which is derived via the temperature difference of the mean temperature of the hot pocket and the ambient fluid $\overline{\Delta T}$ as $\overline{\Delta\rho} = \alpha\rho\overline{\Delta T}$. Substituting these values into the definition of [18]

$$\Psi = \frac{g d \Delta\rho}{3\sigma_0} \tag{13}$$

with $d = 2r_{eq}$ yields values well above, for our simulations 1.6–3.8 times, the critical value $\Psi_c = 6.85$ given by these authors (cf. Fig. 12). This indicates that $\Psi \geqslant 6.85$ is a necessary but not sufficient criterion, as at the same time the Bingham number also needs to be supercritical ($Bi < 1$).

Plotting the maximum velocity versus the product of the equivalent radius r_{eq} and the maximum shear rate (Fig. 14) yields a good agreement between those two velocities. Thus, treating the thermal anomaly as a hot pocket of radius r_{eq} rising through the fluid is a good approximation.

5.2. Height where the plume stops

In Section 4 we illustrated the effect of the rheological properties of the fluid on the evolution of the thermal instability and found that all parameters strongly influence the height h_y where the plume stops. Fig. 15 summarizes these results for the simulations. Fig. 15 A therefore assembles h_y for all the simulations with

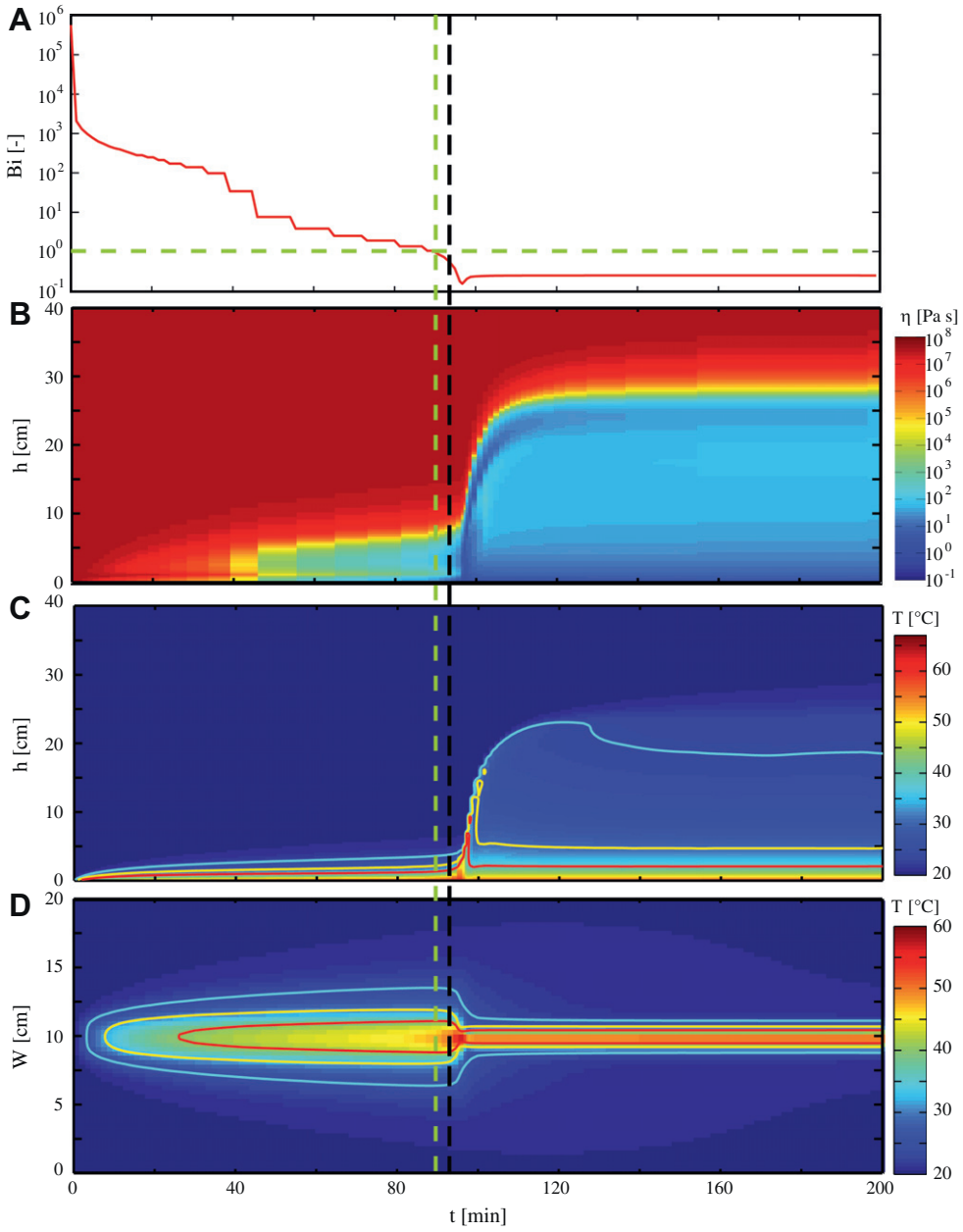

Fig. 11. Different temporal evolutions for simulation 24, cf. Table 1. (A) evolution of the Bingham number $Bi = \frac{\sigma_0}{K_v \dot{\gamma}_{max}^n}$ where $\dot{\gamma}_{max}$ is the maximum shear rate evaluated at each time step. The vertical green line marks $Bi = 1$. (B) Spatiotemporal evolution of the viscosity at the plume axis. (C) Spatiotemporal evolution of the temperature at the plume axis. Red, yellow and blue lines indicate isotherms at $T = 39.9$ °C, $T = 31.1$ °C and $T = 23.9$ °C respectively. (D) Spatiotemporal evolution of the temperature of a horizontal line through the thermal boundary layer and the plume axis. The vertical black dash-dotted line indicates when the Bingham number in A becomes one, the vertical green line indicates when the $T = 39.9$ °C – isotherm in D starts to deform. (For interpretation of the references to colour in this figure legend, the reader is referred to the web version of this article.)

$Y_0 < 1000$. For higher Y_0 the plume always arrives at the surface. The highlighted series (green □, $K_v = 1.403$ Pa s^n, $n = 0.58$ and varying σ_0) will now be discussed. With increasing yield parameter Y_0, we can observe that h_y first decreases and then increases again. We therefore compare two simulations that stop at approximately the same height but are on either branch of that curve (cf. points marked as PI and PII in Fig. 15). For each simulation we visualized the evolution of the viscosity on the plume axis through time (Fig. 15C1 and C2). The plume at lower yield parameter, PI with $Y_0 = 245.1$, starts much later than PII ($Y_0 = 476.2$). Once it starts, PI is much faster than PII, as shown by the maximum velocity (Fig. 15B), which is 1.5 times higher for PI than for PII. This can be explained by PI having accumulated much more buoyancy than PII, as it was heated for a longer time. In Fig. 14 we can see that a plume with a higher shear thinning exponent (comparing red points with $n = 0.7$ to blue points with $n = 0.5$) rises much faster. Fig. 15A and B show that these faster plumes also rise higher (higher h_y). However this does not explain why the plume stops and how the transition from the left to the right branch of Fig. 15 takes place.

A plume rises if it is buoyant enough, and as we could see at the onset, the Bingham number has to be supercritical ($Bi < 1$). We therefore calculate in a first step the Bingham number along the plume axis through time (Fig. 15D) using the local shear rates and the respective fluid parameters. Comparing this evolution for each fluid shows that the Bingham number for PI becomes subcrit-

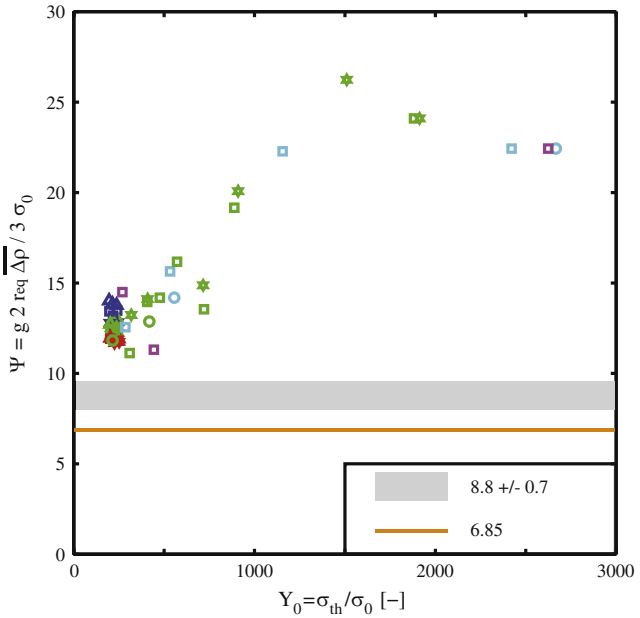

Fig. 12. Yield number Ψ with mean density difference $\overline{\Delta\rho}$ between mean density of hot pocket with radius r_{eq} and ambient fluid at plume onset versus yield parameter. Orange line indicates $\Psi = 6.85$ [17–20] and grey bar corresponds to $\Psi = 8.8 \pm 0.7$ [12]. (For interpretation of the references to colour in this figure legend, the reader is referred to the web version of this article.)

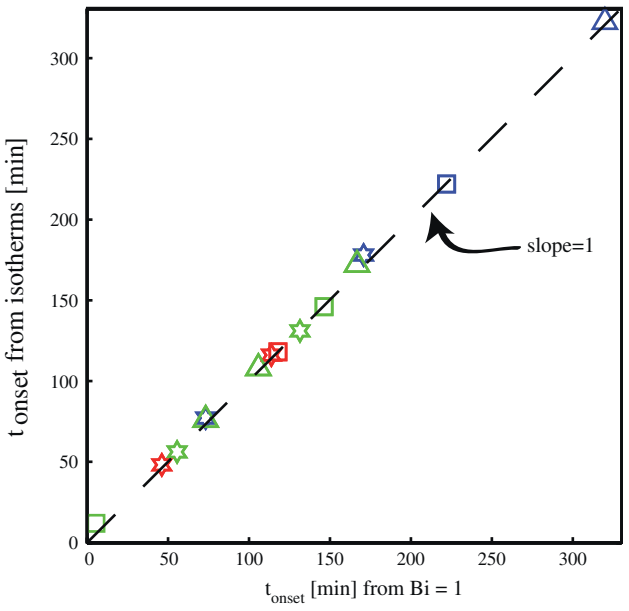

Fig. 13. Onset time determined from spatiotemporal evolution of a horizontal pixel line of the temperature field in the thermal boundary layer versus onset time determined from the criterion $Bi = 1$. Colour convention as in Fig. 5.

ical ($Bi > 1$) at the plume head as the plume stops. On the other end PII stops even though its Bingham number is still supercritical. In a second step we now calculate the local yield number Ψ, with the maximum temperature difference between head of the plume and ambient fluid and r_{eq} as determined for the onset. We find that as PII stops, the yield number becomes $\Psi = 5.124$, which is below the critical value of $\Psi = 6.85$ given by [17–20] and also the one determined experimentally for the thermal instability in Carbopol by [12].

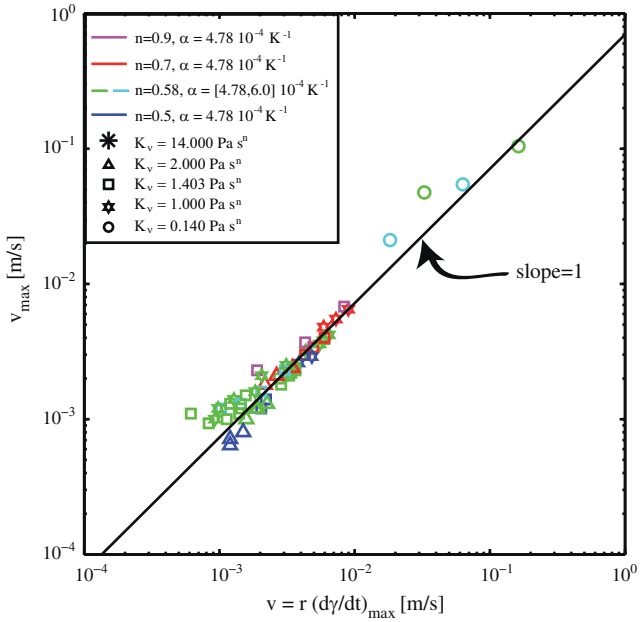

Fig. 14. Maximum velocity v_{max} during plume uplift versus radius of hot pocket times maximum shear rate during plume uplift. The radius has been evaluated from the size of the thermal boundary layer at the onset of the plume, as described in [12]. The black line indicates a slope equal to one.

If we do this analysis for all data points, we find simulations in which the Bingham number is already subcritical while the yield number Ψ is still supercritical and vice versa. This indicates that, as soon as Bi or Ψ become subcritical, the plume stops rising. The critical yield number is $\Psi_c = 5 \pm 1.2$. This uncertainty is due to the fact that we are not saving every field at every time step.

We then determined for each simulation, which parameter becomes subcritical first, i.e. whether it is the Bingham or the yield number that causes the plume to stop, and the time t_s when the respective parameter becomes subcritical. At t_s we now determined the value of the other parameter, which is still super critical at this time. The results are plotted against the yield parameter Y_0 (Fig. 16) where the filled symbols show the yield number Ψ (when the Bingham number becomes subcritical) and the open symbols the Bingham number (when the yield number becomes subcritical).

The plot (Fig. 16) is divided into two parts, where separation occurs at $Y_0 = Y_{0c} \approx 300$, corresponding to the minimum observed in Fig. 15A. Approaching $Y_{0c} = 300$ the yield number approaches the critical value ($\Psi \to \Psi_c$) and the Bingham number $Bi \to Bi = 1$.

Besides the differences for h_y, we can observe that the morphology of the plume changes from the left to the right branch (Fig. 15E). On the left branch, where the dynamics are dominated by the Bingham number, the strongest deformation occurs at the edges of the instability. Around the plume axis, deformation is low ($\dot{\gamma} < 10^{-3}\ s^{-1}$) and inside the instability as well (Fig. 15D1). The transition from the edges of the instability towards the inside is rather sharp, compared with (Fig. 15D2 and Fig. 15E2) PII on the right branch, where it is more smeared out. For PII the deformation pattern resembles much more the pattern observed in a Newtonian or purely shear thinning fluid.

6. Conclusions

We performed a systematic numerical study on the influence of the rheological properties in a regularized Herschel–Bulkley fluid on the development of thermal instabilities produced by a small

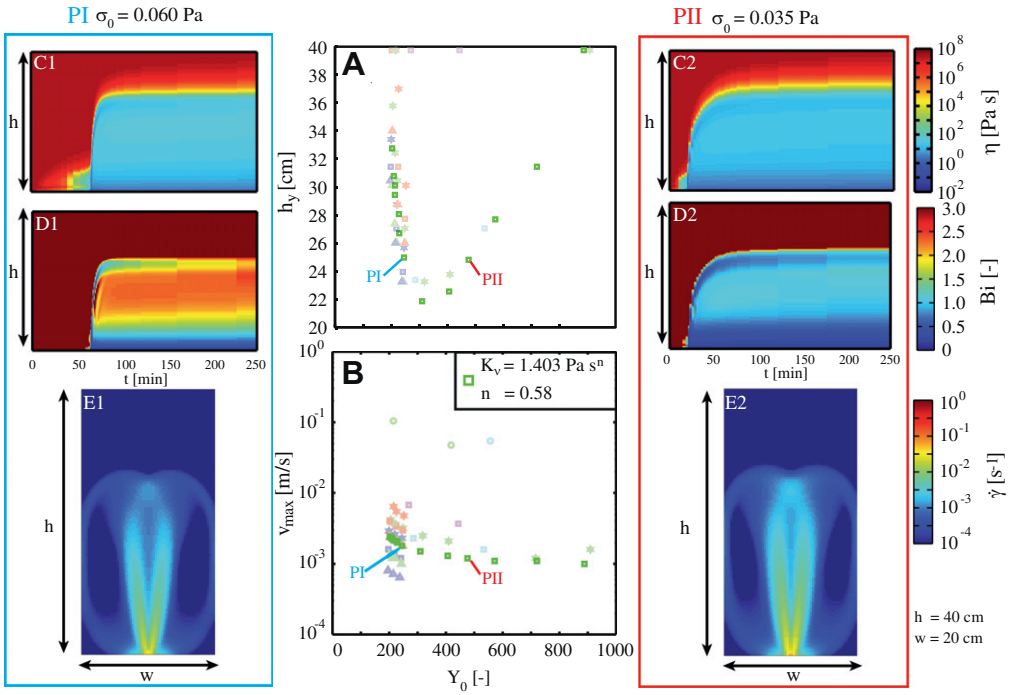

Fig. 15. Height h_y (A) and maximum velocity (B) versus yield parameter. Dark green boxes show simulations for $K_v = 1.403$ Pa s^n and $n = 0.58$, transparent values shown for comparison with colour convention as in Fig. 5. (C) spatiotemporal evolution of the viscosity at plume axis. (D) spatiotemporal evolution of the Bingham number at the plume axis. (E) vertical cross section of the shear rate at the plume axis, shear rate limited from $\dot{\gamma} = 10^{-4}$ s^{-1} to $\dot{\gamma} = 10^{0}$ s^{-1} to highlight the different morphology. (For interpretation of the references to colour in this figure legend, the reader is referred to the web version of this article.)

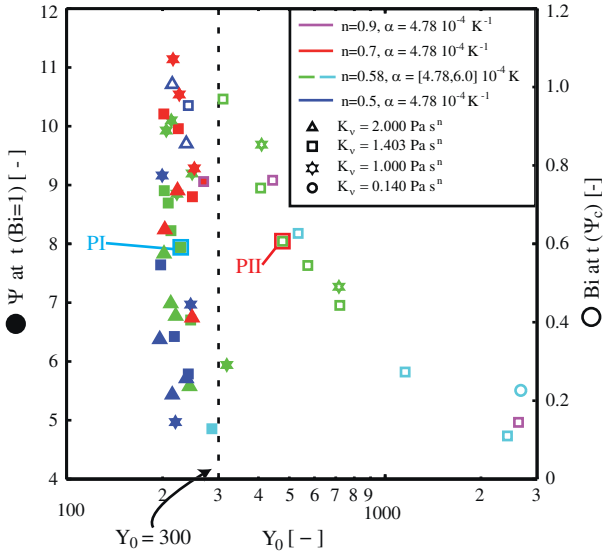

Fig. 16. Yield number ($\Psi = \Delta\rho g 2r_{eq}/3\sigma_0$, filled symbols) at the time when, at the plume head, the Bingham number passes $Bi = 1$ and Bingham number (empty symbols) at the time when the yield number passes critical value $\Psi_c = 5 \pm 1.2$ versus yield parameter ($Y_0 = \alpha\rho g\ P/k\sigma_0$). For low yield parameter ($Y_0 < 300$) the Bingham number is the parameter that evokes a stopping of the plume, while Ψ is still supercritical. For higher yield parameter ($Y_0 > 300$) the stopping of the plume is caused by a loss of sufficient buoyancy, therefore Ψ becomes subcritical, while the Bingham number is still super critical ($Bi < 1$).

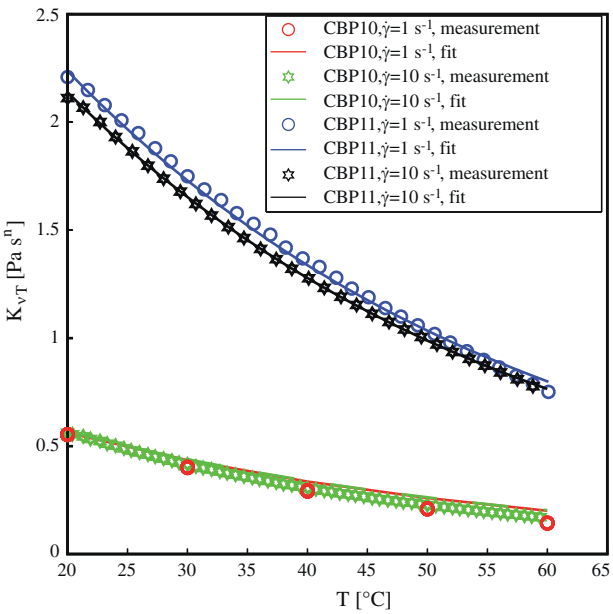

Fig. 17. Dependence of consistency K_{vT} on temperature T. Rheological properties measured in flow test for CBP10: $\sigma_0 = 0.018$ Pa, $K_v = 0.75$ Pa s^n, $n = 0.62$ and for CBP11: $\sigma_0 = 0.1$ Pa, $K_v = 1.5$ Pa s^n, $n = 0.5$. Measurements are fitted with $K_{vT} = K_v a\ e^{-bT}$, with $A = 1.6927$ and $B = -0.0257$ K^{-1}.

heated patch. The comparison with laboratory experiments shows that the purely viscous description of [26] is adequate to describe the plume onset and its development. In agreement with [12], we find that the yield parameter $Y_0 = \alpha\rho g\ P/k\sigma_0$ is the key external parameter to describe the transition from a slowly convecting hot cell around the heater towards a rising plume. Its critical value depends on the heater geometry and is $Y_{0c} = 165 \pm 25$ for a heater flush-mounted on the bottom of the tank. In addition, the determination of the 3D temperature, velocity, shear stresses and viscosity

fields allows us to show that there are two necessary local conditions for a plume to take off and continue to rise. First, the local buoyancy of the hot pocket of fluid should be greater than the yield stress (which implies that $\Psi = \Delta\rho g 2 r_{eq}/3\sigma_0 \geqslant \Psi_c = 5 \pm 1.2$). Second, the Bingham number, which compares the yield stress to the viscous stresses, $Bi = \sigma_0/K_v\dot{\gamma}^n$, should be smaller than 1.0. This implies that the local shear rate should be greater than a characteristic shear rate scale that only depends on the rheological properties of the fluid. As soon as $\Psi < \Psi_c$ or $Bi > 1$, the plume stops its upwards progression. Hot material will continue to rise from the bottom of the tank but it will spread under an unyielded, high viscosity region at the top of the box. Further work is now under way to characterize plume dynamics in steady state.

Acknowledgments

The work has benefited from discussions with François Boulogne, Georg Dietze and Fabien Mahaut and help in the laboratory from Floriane Touitou, Alban Aubertin and Lionel Auffray. The manuscript was improved, thanks to the comments of two anonymous reviewers. A. Massmeyer and T. Rolf are supported by the Initial Training Network (ITN) Crystal2Plate, an FP7-funded Marie Curie Action under grant agreement number PITN-GA-2008-215353. E. Di Giuseppe was funded by the French Agence Nationale de la Recherche (PTECTO NT09-604042).

Appendix A. Temperature dependence of the consistency

The temperature dependence for K_{vT} has been evaluated performing a temperature sweep test at constant shear rate. To verify the uniformness of the model, we used two different mixtures of Carbopol (for rheological properties see figure caption Fig. 17) and applied two different shear rates $\dot{\gamma} = 1\ \mathrm{s}^{-1}$ and $\dot{\gamma} = 10\ \mathrm{s}^{-1}$. The results are plotted in Fig. 17. The figure shows that the model $K_{vT} = K_v A\, e^{-B\,T}$ with the coefficients $A = 1.6927$ and $B = -0.0257\ \mathrm{K}^{-1}$ fits the data reasonably well, for both fluids and at both shear rates.

References

[1] J.C.R. Hunt, Industrial and environmental fluid mechanics, Annu. Rev. Fluid Mech. 23 (1991) 1–41.
[2] J.F. Steffe, Rheological Methods in Food Process Engineering, Freeman Press, 1996. ISBN 9780963203618.
[3] V.A. Solomatov, A.C. Barr, Onset of convection in fluids with strongly temperature-dependent, power-law viscosity, Phys. Earth Planet. Int. 155 (2006) 140–145.
[4] J. Zhang, D. Vola, I.A. Frigaard, Yield stress effects on Rayleigh–Bénard convection, J. Fluid Mech. 566 (2006) 389–419.
[5] N.J. Balmforth, A.C. Rust, Weakly nonlinear viscoplastic convection, J. Non-Newton. Fluid Mech. 158 (2009) 36–45.
[6] A. Vikhansky, Thermal convection of a viscoplastic liquid with high Rayleigh and Bingham numbers, Phys. Fluids 21 (2009) 103103, http://dx.doi.org/10.1063/1.3256166.
[7] A. Vikhansky, On the onset of natural convection of Bingham liquid in rectangular enclosures, J. Non-Newton. Fluid Mech. 165 (2010) 1713–1716.
[8] A. Vikhansky, On the stopping of thermal convection in viscoplastic liquid, Rheol. Acta 50 (2011) 423–428.
[9] O. Turan, N. Chakraborty, R.J. Poole, Laminar natural convection of Bingham fluids in a square enclosure with differentially heated side walls, J. Non-Newton. Fluid Mech. 165 (2010) 901–913.
[10] O. Turan, N. Chakraborty, R.J. Poole, Laminar Rayleigh–Bénard convection of yield stress fluids in a square enclosure, J. Non-Newton. Fluid Mech. 171–172 (2012) 83–96.
[11] A.C. Barr, R.T. Pappalardo, S. Zhong, Convective instability in ice I with non-Newtonian rheology: application to the icy Galilean satellites, J. Geophys. Res. 109 (2004) E12008.
[12] A. Davaille, B. Gueslin, A. Massmeyer, E. Di Giuseppe, Thermal instabilities in a yield stress fluid: existence and morphology, J. Non-Newton. Fluid Mech. (in press) <http://dx.doi.org/10.1016/j.jnnfm.2012.10.008>.
[13] J.M. Piau, Carbopol gels: elastoviscoplastic and slippery glasses made of individual swollen sponges: Meso- and macroscopic properties, constitutive equations and scaling laws, J. Non-Newton. Fluid Mech. 144 (2007) 1–29.
[14] P. Coussot, L. Tocquer, C. Lanos, G. Ovarlez, Macroscopic vs. local rheology of yield stress fluids, J. Non-Newton. Fluid Mech. 158 (2009) 85–90.
[15] F. Oppong, J. de Bruyn, Mircorheology and jamming in a yield-stress fluid, Rheol. Acta 50 (2011) 317–326. ISSN: 0035-4511. <http://dx.doi.org/10.1007/s00397-010-0519-9>.
[16] T. Divoux, C. Barentin, S. Manneville, From stress-induced fluidization processes to Herschel–Bulkley behaviour in simple yield stress fluids, Soft Matter. 7 (2011) 8409–8418, http://dx.doi.org/10.1039/C1SM05607G.
[17] N. Dubash, I.A. Frigaard, Conditions for static bubbles in viscoplastic fluids, Phys. Fluids 16 (2004) 4319–4330.
[18] N. Dubash, I.A. Frigaard, Propagation and stopping of air bubbles in Carbopol solutions, J. Non-Newton. Fluid Mech. 142 (2007) 123–134.
[19] A.N. Beris, J.A. Tsamopoulos, R.C. Armstrong, R.A. Brown, Creeping motion of a sphere through a Bingham plastic, J. Fluid Mech. 158 (1985) 219–244.
[20] H. Tabuteau, P. Coussot, J.R. de Bruyn, Drag force on a sphere in steady motion through a yield-stress fluid, J. Rheol. 51 (2007) 125–137.
[21] A. Davaille, A. Limare, F. Touitou, I. Kumagai, J. Vatteville, Anatomy of a laminar starting thermal plume at high Prandtl number, Exp. Fluids 50 (2011) 285–300.
[22] B. Gebhart, Effects of viscous dissipation in natural convection, J. Fluid Mech. 14 (1962) 225–232.
[23] T.B.C. Divoux, T. David, S. Manneville, Transient shear banding in a simple yield stress fluid, Phys. Rev. Lett. 104 (2010) 1–4.
[24] A.N. Alexandrou, T.M. McGilvreay, G. Burgos, Steady Herschel–Bulkley fluid flow in three-dimensional expansions, J. Non-Newton. Fluid Mech. 100 (2001) 77–96.
[25] H. Zhu, Y. Kim, D.D. Kee, Non-Newtonian fluids with a yield stress, J. Non-Newton. Fluid Mech. 129 (2005) 177–181. ISSN: 0377-0257.
[26] P.R. de Souza Mendes, E.S.S. Dutra, Viscosity function for yield-stress liquids, Appl. Rheol. 14 (2004) 296–302.
[27] P.R. de Souza Mendes, M.F. Naccache, P.R. Varges, F.H. Marchesini, Flow of viscoplastic liquids through axisymmetric expansions-contractions, J. Non-Newton. Fluid Mech. 142 (2007) 207–217.
[28] P.J. Tackley, Three Dimensional Models of Mantle Convection: Influence of Phase Transistions and Temperature-Dependent Viscosity, Ph.D. thesis, California Institute of Technology, Pasadena, 1994.
[29] P.J. Tackley, Effects of strongly temperature-dependent viscosity on time-dependent, three-dimensional models of mantle convection, Geophys. Res. letters 20 (1993) 2187–2190.
[30] P.J. Tackley, Effects of strongly variable viscosity on three-dimensional compressible convection in planetary mantles, J. Geophys. Res. 101 (1996) 3311–3332.